Microporous and Mesoporous Materials 360 (2023) 112712

Contents lists available at ScienceDirect

Microporous and Mesoporous Materials

journal homepage: www.elsevier.com/locate/micromeso

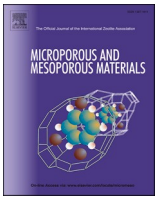

MOF-alumina composites for improved methane adsorption under wet conditions

David Ursueguía, Eva Díaz, Salvador Ordóñez *

Catalysis, Reactors and Control Research Group (CRC), Department of Chemical and Environmental Engineering, University of Oviedo, Julián Clavería S/n, 33006, Oviedo, Spain

ARTICLE INFO

Keywords:
HKUST-1 MOF
γ-Al_2O_3 composite
MOF stability
Methane adsorption
Water effect

ABSTRACT

HKUST-1 MOF is considered among the most promising materials for methane adsorption. However, the huge decrease in adsorption capacity under humid conditions, due to water hydrolysis of the structure and blockage of open metal sites, decreases its potential. To address this issue, composites of HKUST-1 and γ-Al_2O_3 particles were synthesized and tested for methane adsorption. MOF impregnation on large particles reduces the pressure drop through the fixed-bed, whereas the known hydrophilicity of the alumina is expected to minimize the water damage to the MOF. Impregnation was performed using two different methods (drip impregnation and solvothermal) with different HKUST-1/Al_2O_3 initial mass ratios (0.05–1.29 g/g) in a PTFE autoclave. The loading, dispersion and main morphological features were confirmed by PXRD, XPS, SEM, BET, DRIFT and TGA. Water influence was determined by ageing samples in a fixed bed under air with 100% RH for 24 h and 3 consecutive cycles, and methane adsorption capacity was checked before and after the humid treatment. Adsorption capacity of HKUST-1 decreases by about 37%, while composites with low MOF loads (<9%) withstand and even improve the methane adsorption capacity by more than 38%. This effect is more noticeable for a more heterogeneous MOF distribution on the alumina surface, following a similar principle to the methane hydrate formation through a surface promoter, but at milder conditions. Surprisingly, these composites also show a significant improvement in thermal stability.

1. Introduction

HKUST-1, $Cu_3(C_9H_3O_6)_2$, known commercially as Basolite C300, is a promising material for gas adsorption and separation, establishing a benchmark in methane adsorption [1]. In fact, previous works have demonstrated its ability to concentrate methane from low-grade streams on a fixed bed [2]. Methane molecules, with considerable polarizability, are selectively attracted to the open metal sites (OMS) of the structure above other major components of the stream, such as nitrogen. HKUST-1 has been synthesized and studied in many published articles, showing very good performance under different scenarios, but in most cases at laboratory scale and mild conditions [3]. However, the scaling-up of processes based on these materials is still challenging.

The first handicap to overcome is the detrimental effect of the moisture on MOF performance [4,5]. The presence of water leads to the hydrolysis of organic ligands within the MOF's structure and a strong affinity towards OMS, resulting in the adsorption sites obstruction and hindering the practical application of HKUST-1 in large-scale processes [6]. Consequently, there has been a growing interest in enhancing the water stability of this material. Initially, various modifications were proposed for the original MOF synthesis route. For instance, Goyal et al. [7] introduced iron (Fe^{3+}) ions into the structure, while Wu et al. [8] incorporated glycine, and Kanno et al. [9] synthesized the MOF through plasma in the liquid phase. Although these alterations yielded improvements, they also induced changes in the MOF's morphological and crystalline structure, making them challenging and expensive to implement, particularly on a large scale. More recently, researchers have suggested the synthesis of composites by combining post-synthetic HKUST-1 with another material, which allows for the preservation of the MOF's structure and simplification of the synthesis process. In this vein, Pan et al. [10] have deposited graphene oxide on the surface of HKUST-1, and Majaz et al. [11] have crystallized HKUST-1 within the mesoporous cavities of silica FDU-12. Despite the promising outcomes, most of these composites are created using costly materials such as graphene or techniques that consume significant energy, like electrodeposition [12,13]. Consequently, these factors contribute to

* Corresponding author.
E-mail address: sordonez@uniovi.es (S. Ordóñez).

https://doi.org/10.1016/j.micromeso.2023.112712
Received 26 May 2023; Received in revised form 15 June 2023; Accepted 19 June 2023
Available online 19 June 2023

excessively high costs, also hampering the potential industrial-scale synthesis of these materials.

One of the major obstacles hindering the industrial application of HKUST-1 is the substantial pressure drop associated with fixed-bed adsorption processes, primarily due to its fine powder form during synthesis and manufacturing [3]. To address this issue, a commonly employed and cost-effective technique is the palletisation of HKUST-1 through mechanical pressure [14]. Shaping the material into larger pills or pellets helps reduce the pressure drop and enhances particle density, which can be advantageous for certain gas adsorption and storage applications [15]. However, palletisation has been found to cause structural amorphization and a significant decrease in the adsorption capacity of HKUST-1. These effects are attributed to a notable reduction in specific surface area and total pore volume, leading to the collapse of micropores [16,17]. HKUST-1 has also demonstrated challenges in forming large structures, which could potentially alleviate the issues associated with pressure drop. In fact, it is not stable in the commonly used dispersion solvents for binders [17]. Consequently, one possible solution that addresses both the harmful effects of moisture and the pressure drop is the combination of HKUST-1 with another material in a composite, aiming to improve its mechanical properties. Therefore, an ideal material for this purpose would be one that can be easily shaped into larger particles, such as commercially available extrusions of common catalyst supports like alumina (Al_2O_3) or silica (SiO_2). Although this approach has been tested in the design of membranes for small molecule separation and enhancing thermal resistance in catalytic reactions, its application in fixed-bed adsorption and gas separation processes has received limited attention [18,19].

The objective of this study is to prepare composites of HKUST-1 and alumina to reduce pressure drop and mitigate the effects of moisture in adsorption processes. The primary goal is to identify an economical and straightforward approach to achieve these improvements. Methane adsorption is used as a reference (probe molecule) due to its favourable results under mild conditions and in small fixed-bed setups, although there are no previous records of scaling up [2]. Impregnation of HKUST-1 onto large alumina particles (355–710 μm) is carried out using solvothermal and drip impregnation methods. Alumina is a cost-effective and easily pelletizable material with high hydrophilicity. The larger particle size of alumina is expected to significantly reduce pressure drop, and its hydrophilicity has shown promise in modifying the polar character of porous membranes when combined with alumina particles [20]. Thus, it is anticipated that the composites will exhibit improved resistance to water damage. Solvothermal and drip impregnation methods are selected for their simplicity and low cost, as they are commonly used for MOF impregnation onto mesoporous supports [21]. Successful synthesis and adsorption testing of these composites could represent a significant breakthrough in the practical utilization of HKUST-1, as no previous studies have effectively addressed these challenges in such a simple and cost-effective manner.

2. Materials and methods

2.1. Materials

Alumina (γ-Al_2O_3) pristine pellets were obtained from BASF (CAS: 1344-28-1), with an original particle size of 2 mm. The remaining chemicals were used for the HKUST-1 synthesis: cupric nitrate trihydrate, $Cu(NO_3)_2{\cdot}3H_2O$, purchased from CAYMAN Chemical Company, trimesic acid, $C_9H_6O_6$, purchased from PRS PANREAC, ultrapure ethanol (99.99%), C_2H_5OH, purchased from VWR Chemicals, and distilled water, H_2O. All the gases used (air, methane, nitrogen and helium) were supplied by Air Liquide with purities above 99.995% mol.

2.2. Synthesis of HKUST-1/Al_2O_3

Firstly, Al_2O_3 particles, between 355 and 710 μm, were obtained by crushing in a mortar and a subsequent sieving of the original alumina pellets (2 mm). On the other hand, HKUST-1 was synthesized through the procedure indicated by Gascon et al. [22]: 0.875 g of $Cu(NO_3)_2{\cdot}3H_2O$ were diluted in 12 ml of distilled H_2O, whereas 0.42 g of $C_9H_6O_6$ were diluted in 12 ml of C_2H_5OH. Both solutions were mixed and stirred for 30 min at ambient conditions. The final mixture was introduced into a PTFE autoclave of 100 ml and heated in an oven at 383 K for 18 h. The product was filtered and threefold washed with distilled water. Finally, resulting material was introduced into the oven at 383 K overnight, obtaining a fine dark-blue powder.

For the synthesis of HKUST-1/Al_2O_3 composites, two different methodologies were used (Fig. S1). Firstly, the solvothermal method [23]: 2.02 g of alumina particles were mixed with the precursors of HKUST-1 in the same proportions as above, and the mixture was taken to the PTFE autoclave (383 K, 18 h). The product was washed with distilled water and filtered. Secondly, the drip impregnation method [22]: 2.02 g of alumina particles were impregnated dropwise with the liquid obtained from the filtration of HKUST-1 (mother liquor) and taken to an oven at 393 K, until the complete solvent evaporation. Then, particles were washed with ethanol and filtered. The product was introduced into the PTFE autoclave with the HKUST-1 precursors (383 K, 18 h) and subsequently washed with distilled water and filtered.

Some modifications have been made to the procedures described above. Alumina quantity was reduced to 1 g in all cases, the total contact volume in the autoclave has been modified to 3 different values (1, 2.4 and 24 ml), and the original concentration of the precursors of HKUST-1 in the contact volume was modified in some cases (100 and 10%). In this way, six different composite materials were synthesized for the process. Nomenclature indicates by numbers (100, 240 and 2400) the amount of MOF in the contact volume, and by letters (v and V) the total contact volume (Table 1).

Once synthesized, the amount of MOF impregnated on alumina for each sample was estimated by thermogravimetry decomposition. Thermograms were obtained on a thermobalance TGA 55 (TA Instruments) for 15–30 mg of each sample, under nitrogen atmosphere (40 ml/min) and a temperature ramp of 5 K/min from ambient temperature to 800 K. At this temperature, the residual mass corresponds to either the inorganic support or the metal of the MOF. Therefore, by using a system of two algebraic equations that account for the total mass of the sample before and after the thermal treatment, and where the independent variables represent the mass of alumina and MOF in the original sample, the MOF loading of each composite can be determined. The accuracy of the measurements according to the manufacturer is: temperature accuracy, ±1 K, and weighing precision, ±0.01%. Additionally, experiments were duplicated.

2.3. Adsorbents characterization

The textural features of specific surface area and pore volume were obtained by nitrogen physisorption at 77 K in a Micromeritics ASAP 2020 surface area and porosity analyser. Physisorption data were processed using Brunauer-Emmett-Teller (BET), Barrett-Joyner-Halenda (BJH) and Dubinin-Radushkevich (DR) approaches for determining surface area, total mesopores and micropores volume, respectively. The

Table 1
Different materials synthesized and the corresponding nomenclature used.

Nomenclature	Procedure	Contact volume (ml)[a]	Precursors (%)[b]
DI_{100v}	drip impregnation	1	100
DI_{240}	drip impregnation	2.4	100
DI_{240V}	drip impregnation	24	10
S_{240}	solvothermal	2.4	100
S_{2400V}	solvothermal	24	100
S_{240V}	solvothermal	24	10

[a] Total volume of liquid in the autoclave.
[b] Concentration respect to the original precursors of HKUST-1 [22,23].

total volume of pores is the sum of both values (BJH and DR). Pore size distributions were obtained using Horvath-Kawazoe method for MOF-containing materials (due to the relevance of microporous contribution) and BJH for the parent alumina.

The surface of the composite samples was analysed by X-ray photoelectron spectroscopy (XPS) using a SPECS system equipped with a Hemispherical Phoibos detector. Scanning electron microscopy (SEM) images and EDX analyses were carried out by using a JEOL 6610LV scanning electron microscope. Samples were coated with gold prior to observation. Infrared spectra were acquired by DRIFT spectroscopy with a Thermo Nicolet FT-IR equipped with a MCT/A detector. The adsorbent sample was placed inside the temperature-controlled chamber. The reflectance measurement was done during the flow of dry-methane. Spectra were recorded in the 650-4000 cm^{-1} wavenumber range, subtracting the correspondent KBr standard background. Finally, the crystallographic structures of the materials were determined by powder X-ray diffraction (PXRD) using a Philips PW 1710 diffractometer, working with the Cu-K_α line ($\lambda = 0.154$ nm) in the 2θ range 5-85° at a scanning rate of 2°/min.

2.4. Adsorption experiments

Pure methane adsorption was evaluated by a thermal gravimetric analyser (TGA 55, TA Instruments). Samples (15–30 mg) were pretreated *in situ* at 423 K and 0.1 MPa in pure nitrogen flowing at 40 ml/min for 2 h. Afterwards, 40 ml/min of methane were flowed at 298 K for 20 h. All weight changes respect to the adsorption data were corrected using a blank calibration. Purge gas was nitrogen flowing continuously at 60 ml/min.

Water ageing of the materials was performed in a stainless-steel tube, 45 and 0.65 cm in length and diameter, respectively. It is filled with 0.15 g of each material. The temperature of the fixed bed was controlled by an electric tubular furnace (Nabertherm). Water was introduced in liquid form by a syringe (Hamilton) of 5 ml powered by a Legato 100 syringe pump (KdScientific), being immediately vaporized due to the action of several isolated heaters along the conductions, at 383 K. The gas flow of air (72 ml/min) was introduced by a mass flow controller (MFC) previously calibrated (Bronkhorst) for 24 h. Operation temperature was 298 K, with a total pressure of 0.1 MPa. Water flowrate was selected according to the relative humidity (RH) desired: 0.2 ml/h for 100% RH, corresponding to 59000 ppm. In the cleaning stage, 72 ml/min of dry air were flowed through the fixed-bed and the temperature was increased up to 423 K for 2 h. Three consecutive water-ageing cycles were applied to each sample. Afterwards, pure methane adsorption capacity was checked again on the thermobalance (20 h, 298 K). Subsequently, a thermal decomposition up to 873 K was carried out for all the samples (N_2, 5 K/min, 40 ml/min, 0.1 MPa), analysing the effluent gases by a mass spectrometer Pfeiffer Vacuum Omnistar previously calibrated. All the adsorption experimentation was done at least twice.

3. Results and discussion

3.1. Adsorbents characterization

The MOF content of composites was calculated by thermal decomposition (**Fig. S2**), considering that the residual mass by comparison with pristine materials. Table 2 shows the MOF content of each of the studied materials. HKUST-1 shows a slight loss of mass at low temperatures, related to water physisorbed, and a next collapse of the structure by means of the breakage of the organic ligand at 593 K, with a mass loss around 45%. In case of alumina, only a loss related to water linked to the surface (11%) is registered in the whole temperature range. All the composite decomposition curves obtained are intermediate between alumina and HKUST-1, being closer to the alumina. Interestingly, it is observed that the collapse of the organic ligand of the MOF occurs at higher temperature for composite materials, around 650 K, and in a less abrupt way than in the case of pristine HKUST-1. This change in the thermograms is consistent with the results obtained by other authors, in which the synthesis of composites with HKUST-1 achieve more thermally stable materials [24]. The bonds between the MOF and the support strengthen the whole composite structure.

Table 2
Main features of the considered materials.

Material	% HKUST-1[a]	BET (m^2/g)	Micropore volume (cm^3/g)	Mesopore volume (cm^3/g)
HKUST-1	100	1680	0.723	0.110
Al_2O_3	0	246	0.0062	0.498
DI_{100v}	1.0	300	0.028	0.498
DI_{240}	17	445	0.057	0.582
DI_{240V}	6.6	278	0.021	0.479
S_{240}	8.6	319	0.038	0.498
S_{2400V}	36	550	0.112	0.299
S_{240V}	4.4	247	0.021	0.420

[a] From thermogravimetry.

Nitrogen physisorption isotherms are shown in Fig. S3. Pristine HKUST-1 exhibits a type-I adsorption isotherm, with a pronounced increase at low partial pressures (~500 cm^3/g), which is indicative of the large importance of micropores, followed by a flat zone up to $P/P_0 = 1$. For the composite materials, intermediate curves between the MOF and the alumina are observed. In fact, the specific surface area follows the same order as the MOF amount on the alumina, Table 2, showing the large contribution of the MOF to the available surface of the composite, with less influence on the total pore volume. Consequently, the higher the amount of MOF in the composite, the greater adsorption in the area corresponding to low partial pressures, related to the micropores importance. This effect is especially relevant in the case of S_{2400V}, with 36.6% HKUST-1. However, all the isotherms correspond to a type-IV, as alumina, with a hysteresis cycle that indicates the apparition of capillary condensation in the mesopores, add to a characteristic multilayer adsorption. Thus, MOF impregnation does not modify the large mesoporous properties of pristine alumina, except in case of high MOF load, like S_{2400V}. Hence, S_{240V}, with a very low MOF content, exhibits a behaviour very close to alumina.

Fig. 1 shows the influence of MOF loading, obtained by thermogravimetry, on the BET specific surface area of each composite. All the materials follow a linear trend between alumina and HKUST-1 ($R^2 = 0.99$), except S_{2400V} and DI_{100v}. In fact, these composites differ in the

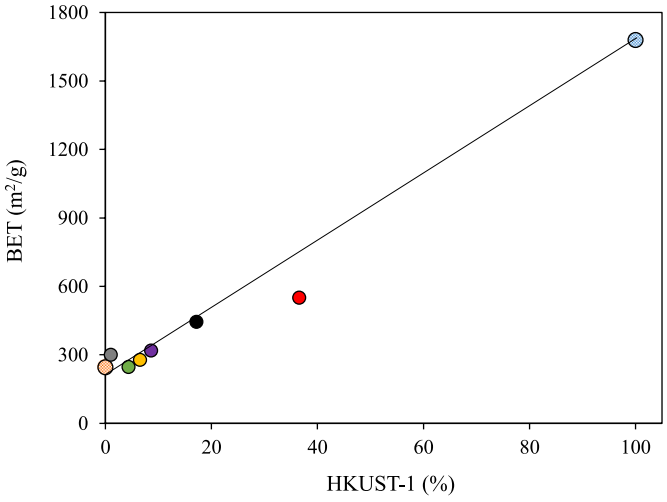

Fig. 1. Relation between the BET specific surface area and the quantity of MOF in each material. HKUST-1 (blue stripped), Al_2O_3 (orange stripped), DI_{240} (black), DI_{100v} (grey), DI_{240V} (yellow), S_{240} (purple), S_{240V} (green) and S_{2400V} (red). Black line guides the view.

synthesis process, since both start with different HKUST-1/Al_2O_3 ratio (1.29 and 0.05 g/g, respectively), whereas in the other cases the ratio remains constant, 0.13 g/g. A similar behaviour was reported by Yang et al. [25] in the synthesis of ZIF-8/CNT composites from values greater than 20% CNT. In fact, limited MOF loadings can be homogeneously distributed on the alumina surface, maximizing the exposed MOF area. However, high MOF/alumina ratio could promote MOF multilayering instead of a thin-layer distribution, with the subsequent blockage of surface and pores, decreasing the surface availability and reducing the adsorption efficiency. Yu et al. [26] described the same effect in the impregnation of TiO_2 with CNTs, with a decrease of available specific surface and morphological properties at high CNTs load. In contrast, other authors refer to the crystal size of HKUST-1 as very decisive in the available BET specific surface area [27]. Therefore, it could be also considered that both the amount of MOF impregnated, as well as the variation of the initial MOF/alumina ratio, influence the crystallization. Differences between both impregnation methodologies are observed in the total pore volume, larger in drip impregnation method (Table 2). It may be due to the recrystallization step in the autoclave for drip impregnation procedure, which enhances the removal of unreacted substances initially blocking the pores of the MOF. Sule et al. [28] previously described this effect in the synthesis of composites of multi-walled carbon nanotubes and HKUST-1. Finally, the pore size distribution of the composite materials calculated by the Horváth-Kawazoe (HK) model is shown in Fig. S4. For the composites prepared by the drip impregnation method, the predominant pore size descends in the following order: DI_{240} (1.40 nm) > DI_{100V} (1.31 nm) > DI_{240V} (1.05 nm), while for those prepared by the solvothermal method, the order will be S_{240V} (1.40 nm) > S_{240} (1.24 nm) > S_{2400V} (0.98 nm), with the latter case showing a band between 3 and 5 nm.

Crystalline structures were obtained by PXRD (Fig. S5). In case of original HKUST-1, a very crystalline structure is observed, with well resolved peaks along the angle range 2θ = 5-45°. The angle position of the main peaks (2θ = 9.5, 11.6, 13.5°) confirms the typical face-centred

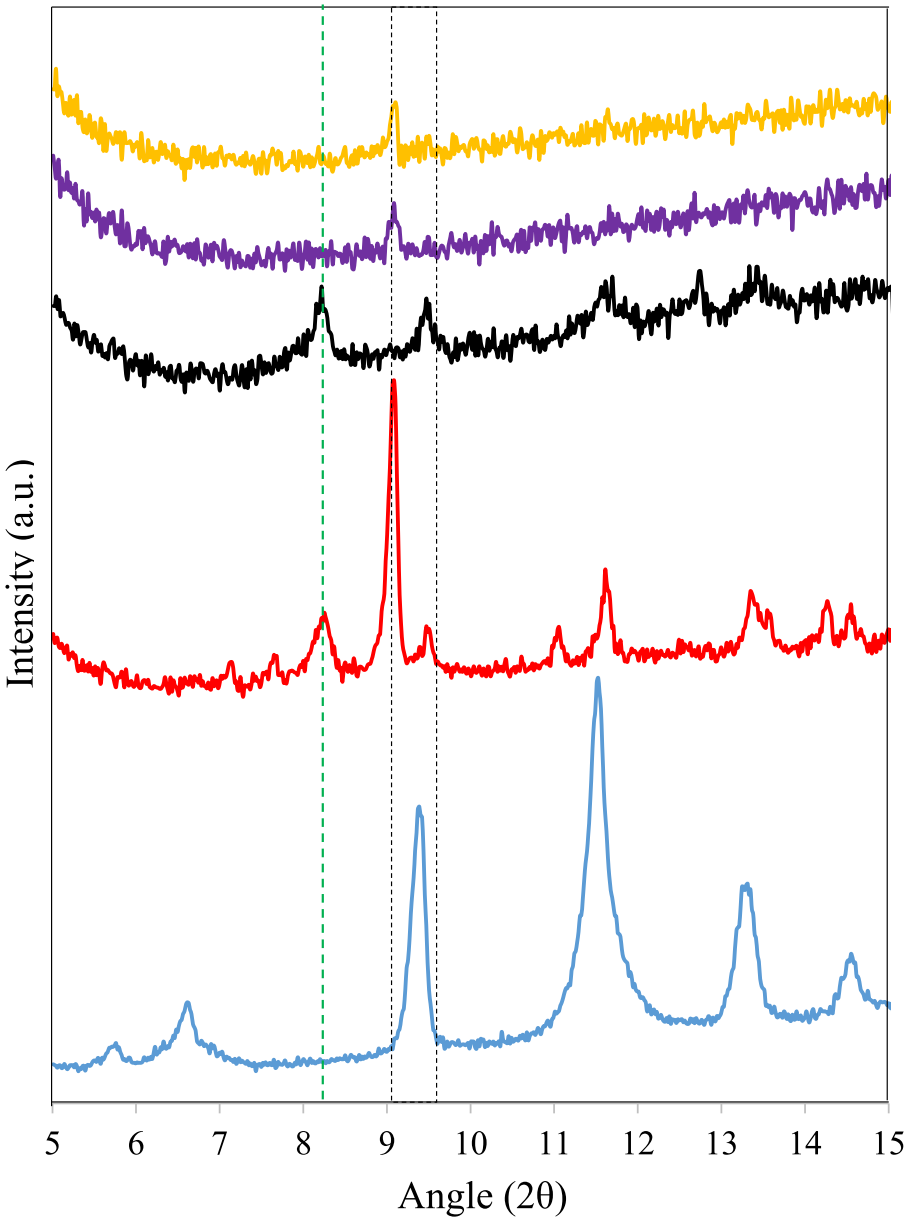

Fig. 2. Low-angle diffractograms of HKUST-1 (blue), S_{2400V} (red), DI_{240} (black), S_{240} (purple) and DI_{240V} (yellow). Discontinuous rectangle points out the original position of the characteristic peak of HKUST-1 taken as reference (9.5°). Discontinuous green line points out the new peak appearance at 8.2°.

cubic (fcc) structure of HKUST-1, elucidated by Miller indexing [16]. On the other hand, the diffractogram of alumina shows an amorphous material, with three wide characteristic peaks at high diffraction angles (2θ = 37, 46, 67°) [29]. Alumina phase is clearly observed for all the composite materials, as it is the main component. However, in the low-angle corresponding to HKUST-1, greater differences are observed between composite materials.

Materials with the highest MOF content show the best defined peaks in the range 2θ = 5-15°. These materials are S_{2400V}, DI_{240}, S_{240} and DI_{240V}, and the intensity of the main peaks follow the same order than MOF amount impregnated on the alumina. Contrary, DI_{100v} and S_{240V} MOF load is very low, and no crystalline phase presence is distinguished by PXRD. Fig. 2 shows a comparative of the main peaks at low angle range for composite materials respect to pristine HKUST-1, where the peak 2θ = 9.5° is taken as reference. For S_{240} and DI_{240V}, it is observed a little shift to lower values (9°), with absence of new diffractogram peaks, and an important intensity loss. According to Emami et al. [30], these little shifts correspond to a preferred crystals orientation on the basal space after the composite formation, and not necessarily to a phase change. In addition, other authors indicate that it can also correspond to an expansion of the unit cell [31], accompanied in this case by a decrease in the crystal size, deduced by the growth of the full width at half maximum (FWHM) of the reference peak, following Scherrer equation. These results suggest that the crystal structure of the MOF is not affected by the composite formation, but it greatly influences the total crystallinity of HKUST-1 when combined with an amorphous material at low loads. Similar results were described by Martak et al. [32] in the study of the combination of HKUST-1 and Al_2O_3 particles.

On the other hand, different patterns are obtained for materials with the highest MOF loadings. Concerning S_{2400V}, it maintains the original crystalline phase, with peaks at 2θ = 9, 11.5 and 13.3°, again with a slight shift respect to pristine HKUST-1. However, the presence of several new small peaks: 9.6, 11, 13.5 and 14° is observed, close to the characteristic HKUST-1 peaks indicated above, pointing out a splitting of these initial ones. Ma et al. [33] obtained similar results, which were attributed to an adequate crystallization of HKUST-1 in combination with high proportion of alumina, which decreases the relative intensity of MOF peaks, leading to this diffraction peaks splitting effect. Surprisingly, in the case of both S_{2400V} and DI_{240}, a new peak appears at 8.2°. To the best of the authors' knowledge, no previously published work on HKUST-1 composites has reported the presence of the new diffractogram peak observed in this study. According to the results presented by Zheng et al. [34], trimesic acid, which is the organic ligand that conforms the structure of HKUST-1, show a characteristic peak at 2θ values around 8°. In fact, a possible combination of trimesic acid and aluminium ions (from alumina particles) may result in MIL-96(Al) MOF, with characteristic diffraction peaks in the environment of 8° [35]. Alternatively, the emergence of the new diffractogram peak could be attributed to alterations in the crystallization pattern occurring at high MOF loads on the alumina substrate. Similarly, other studies have documented similar effects on the crystallization of HKUST-1 when combined with other materials to form composites [36]. XPS analyses were conducted to investigate the electronic properties of the materials under study. High-resolution spectra of C1s, O1s, and Cu2p were deconvoluted to compare the chemical states of these atoms in HKUST-1, Al_2O_3, and the composite materials (Fig. S6A). In case of HKUST-1, C1s spectra show peaks at binding energies of 284 (C═C), 286 (C–O) and 288 (O═C–O) eV, which are characteristic of the trimesic acid. O1s spectra show a main peak at 531 (C–*O*–Cu) eV, characteristic of the structural copper open metal sites. In addition, Cu2p spectra show peaks at binding energies of 934 (Cu^{2+}), 954 (Cu^{2+}), 932 (Cu^{+}) and 952 (Cu^{+}), which demonstrates the presence of copper ions in both possible oxidation states. In case of pure alumina, the absence of peaks in Cu2p spectra clearly indicates that there is no structural copper, as expected. On the opposite, all the composite materials show peaks in the Cu2p spectra, which indicates presence of copper ions in the structure (**Fig. S6B**). Further, it is observed a clear reduction in the counts related to the O1s spectra in composites, which corresponds to a decrease in trimesic acid concentration respect to pure HKUST-1.

This arrangement is tried to be confirmed by scanning electron microscopy (SEM) combined with EDX (Table S1). Comparing composite materials with simple materials images, it is possible to identify HKUST-1 particles on the alumina surface, with different sizes and distribution (Fig. S7). Defined diamond-shaped particles appear for HKUST-1, octahedral structure characteristic of this crystalline material. In contrast, alumina does not show any regular shape, with large agglomeration in certain zones, probably due to the initial crushing. In case of the composite with the lowest MOF content, DI_{100v}, very small particles are observed on the alumina surface, and there is absence of MOF crystals, as it is also obtained by EDX in terms of copper (0.97% Cu). The next composite material, S_{240V}, shows the presence of some crystals (2.04% Cu), with a fairly homogeneous distribution and certain alumina agglomerations. Then, SEM images and MOF content of S_{240} and DI_{240V} are very similar, but the distribution of crystals on the surface is more homogeneous in the solvothermal one. It is demonstrated by differences in the copper content on the surface: 1.25 and 5.19%, respectively. For a given HKUST-1 loading, drip impregnation composites show more MOF-concentrated areas than solvothermal ones. Therefore, it is noteworthy the more homogeneous distribution of MOF particles on alumina in the case of materials synthesized by the solvothermal method.

Finally, and in the same line than PXRD analyses, notable differences are observed in case of DI_{240} and S_{2400V}, the composites with the highest MOF load. Both composites, especially DI_{240}, show a new phase mixed with alumina particles and HKUST-1 crystals, not observed in simple materials case, in the form of elongated fibers or nanotubes (Fig. 3). These results could be attributable to the appearance of the new crystalline phase in these two materials. In fact, some authors have reported that 1,3,5-BTC may be in the shape of fibers in synthesis at high concentration [37]. In addition, the typical morphological shape of MIL-96 (Al) is very similar to the registered in this case [35]. On the other hand, an EDX analysis conducted on an area consisting of these fibers in DI240 revealed a copper content of 7.2%. This suggests the presence of HKUST-1 or even semi-crystalline copper precursors. Interestingly, the morphology of these fibers bears a strong resemblance to $Cu(OH)_2$ nanotubes reported by Zhang et al. [38], which were subsequently utilized as precursors for HKUST-1 by Okada et al. [39]. However, the diffractogram of $Cu(OH)_2$, characterized by distinct peaks at high diffraction angles, does not align with the observed new phase.

3.2. Methane adsorption at mild conditions

Methane adsorption experiences are carried out on a thermobalance at 298 K and 0.1 MPa for 20 h. Results show a pure methane adsorption capacity of 31.8 and 10.6 mg/g for HKUST-1 and Al_2O_3, respectively. For composites, adsorption capacity decreases as both MOF content, crystallinity, specific surface area and mean pore size decrease. However, DI_{100v} (9.84 mg/g) and DI_{240V} (9.12 mg/g) present even worse methane adsorption capacity than simple alumina (Fig. 4), although both materials show an initial kinetic trend coincident with S_{240V}, above alumina. This initial phase corresponds to the methane adsorption by HKUST-1, more selective towards methane than alumina.

Regarding the kinetic behaviour, adsorption curves have been fit to the Langmuir kinetic model (**Equation (1)**), based on the appropriate results obtained for Basolite C300 in a previous work under similar conditions [40]. Adsorption curves are similar in all cases and fit well to the Langmuir kinetic model (Fig. S8), which considers the rate of adsorption proportional to the percentage of unoccupied active sites for adsorption, which in case of methane are predominantly the OMS [41]. Thus, the good fitting suggests that methane adsorption occurs mainly in the MOF.

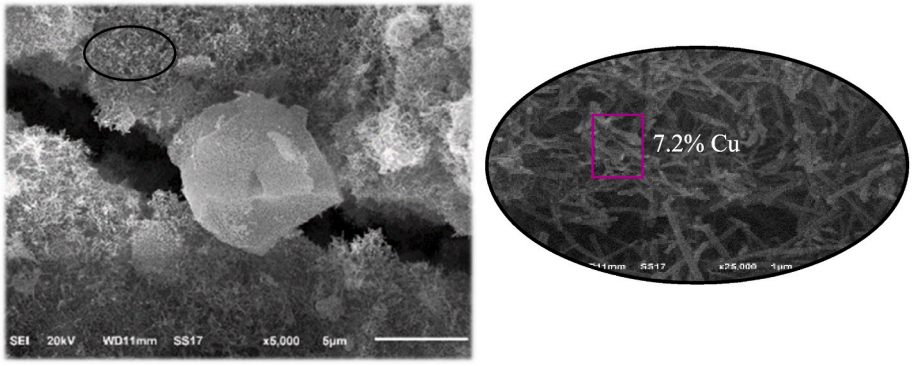

Fig. 3. Enlargement of the DI_{240} SEM image in which the elongated fibers can be seen, and the corresponding EDX analysis of the zone (pink rectangle).

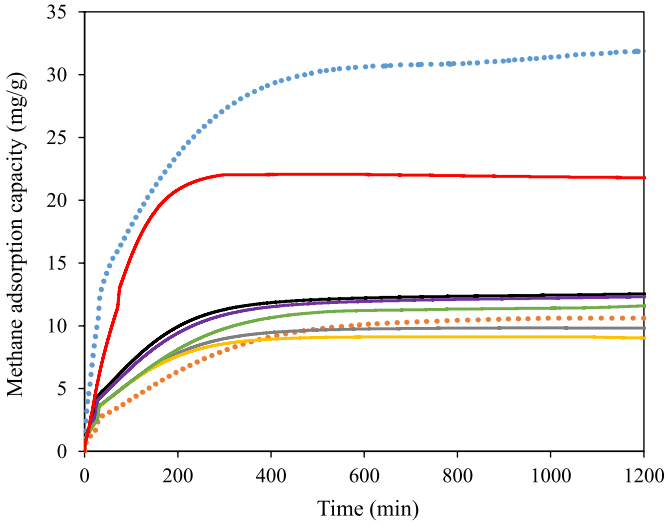

Fig. 4. Methane adsorption curves at 298 K and 0.1 MPa. HKUST-1 (blue striped), Al_2O_3 (orange striped), DI_{240} (black), DI_{100V} (grey), DI_{240V} (yellow), S_{240} (purple), S_{240V} (green) and S_{2400V} (red).

$$q_t = q_e \cdot \frac{k_{ads}}{k_{ads} + k_{des}} \left(1 - e^{-(-k_{ads}+k_{des})t}\right) \quad \text{(Equation 1)}$$

The desorption constant (k_{des}) of the model has been found to be negligible, lower than $9{\cdot}10^{-7}$ s^{-1}, for all the studied materials, and therefore not further considered. Likewise, the k_{ads} decreases as the mean pore diameter of the materials increases. As seen in Table 3, solvothermal composites show higher methane adsorption capacities and lower Langmuir adsorption constants that drip impregnation composites, except in S_{2400V} case. Therefore, it suggests that the MOF impregnated by the solvothermal method is more effective for adsorption than the impregnated by drip impregnation, in agreement with previous results. As shown by SEM analysis, it can be related with the more homogeneous distribution on the surface for solvothermal composites, which proves to be key in adsorption processes of composite materials [42]. Heterogeneity in drip impregnation materials causes faster (higher Langmuir constant) but less effective (lower adsorption capacity) saturation kinetics. In order to corroborate this assumption, Fig. 5 relates the methane adsorption capacity and the load of MOF for each material. The straight line joining HKUST-1 and alumina indicates a linear behaviour between MOF load and adsorption capacity. Materials above the line indicate that the MOF is located on the alumina in an arrangement that favours the adsorption, the opposite in case of materials below the line. As seen, solvothermal materials stay on or above the line, whereas drip impregnation materials stay clearly below the line, especially DI_{240V}.

Table 3
Pure methane adsorption capacity (298 K, 0.1 MPa) and value of Langmuir adsorption constant for each material.

Material	CH_4 capacity (q_e, mg/g)	k_{ads} (s^{-1})	R^2
HKUST-1	32.1 ± 0.6	$1.33{\cdot}10^{-4}$	0.95
Al_2O_3	10.6 ± 0.2	$8.11{\cdot}10^{-5}$	0.99
DI_{100V}	9.84 ± 0.3	$1.45{\cdot}10^{-4}$	0.98
DI_{240}	12.5 ± 0.2	$1.52{\cdot}10^{-4}$	0.97
DI_{240V}	9.12 ± 0.3	$1.68{\cdot}10^{-4}$	0.98
S_{240}	12.3 ± 0.6	$1.29{\cdot}10^{-4}$	0.98
S_{2400V}	22.1 ± 0.4	$2.01{\cdot}10^{-4}$	0.99
S_{240V}	11.6 ± 0.2	$1.11{\cdot}10^{-4}$	0.98

3.3. Fixed-bed performance and ageing in presence of water

In order to test the fixed-bed performance and the water resistance of the materials studied, 72 ml/min of air with 100% RH (59000 ppm) are flowed continuously through a fixed-bed of each material (0.15 g) for 24 h, at 298 K and 0.1 MPa. Firstly, pressure drop of a fixed-bed packed with pristine HKUST-1 (20 μm) was measured, resulting in $4.7{\cdot}10^5$ Pa/m, due to its large compaction and low void space. In contrast, alumina, with much larger particle size (355–710 μm), exhibits a practically negligible pressure drop, $3.1{\cdot}10^4$ Pa/m. The same trend is followed in case of composites, with a particle size similar to alumina, and a pressure drop around $3.2{\cdot}10^4$ Pa/m in all cases. In addition, composite particles do not show attrition when conforming the fixed-bed. Therefore, composite particles perform much better than HKUST-1 in a fixed-bed in

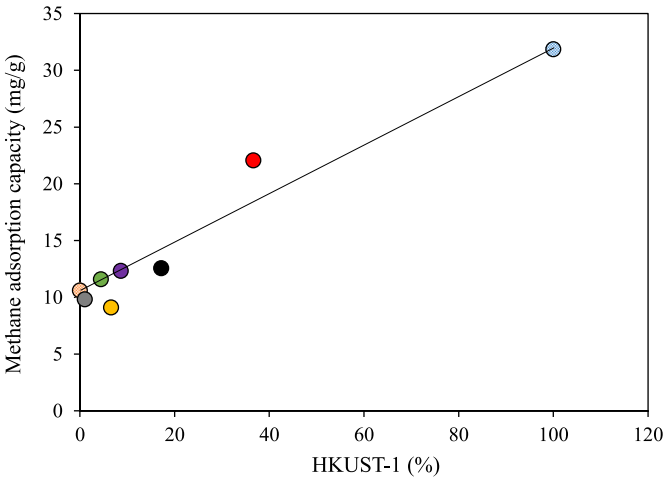

Fig. 5. Relation between pure methane adsorption capacity obtained by thermobalance (298 K, 0.1 MPa) and the MOF load on each composite. HKUST-1 (blue), Al_2O_3 (orange), DI_{240} (black), DI_{100V} (grey), DI_{240V} (yellow), S_{240} (purple), S_{240V} (green) and S_{2400V} (red).

physical terms, in which the pressure drop of the MOF can entail very high associated costs.

Secondly, after the humid treatment for 24 h, materials are treated at 423 K under dry air for 2 h. This procedure simulates an actual adsorption process with an intermediate regeneration cycle at high temperature, similar to a temperature-swing adsorption (TSA) process. Then, methane adsorption capacity is tested in the previous conditions. In case of HKUST-1, the methane adsorption capacity decreases 14.4% respect to the pristine material, whereas alumina shows a loss of 4.8%. As expected, HKUST-1 performance suffers greatly under humid conditions, as water present high attraction towards OMS, reducing the availability of active adsorption sites for methane. On the contrary, alumina withstands the water presence, and shows great hydrophilicity already reported by other authors [43]. HKUST-1 shows a reduction in the Langmuir kinetic constant ($6.4{\cdot}10^{-5}$ s^{-1}), suggesting a slight alteration of the active sites for methane adsorption. The same trend is followed by the composites with the highest MOF loadings, S_{2400V} and DI_{240}, with 5.9 and 9.4% decrease in methane adsorption capacity, respectively. The presence of alumina diminishes a little the water effect, but the MOF continues to be greatly affected. On the contrary, the trend completely shifts by reducing the MOF loading on alumina particles. All the composites with medium and low MOF loading present an increase in methane adsorption capacity (Fig. 6). Further, the capacity increase is larger for drip impregnation composites. This is surprising, since drip impregnation composites are also the materials with the poorest MOF distribution for adsorption, as shown in Fig. 5. This fact suggests that the MOF heterogeneity on the alumina surface increases the MOF stability in presence of water and enhances the methane adsorption capacity, but only at reduced MOF loadings.

Several authors have proposed HKUST-1 as a powerful precursor to methane-hydrate formation, due to its large pore wettability [31,44]. Furthermore, it was demonstrated that it is largely favoured at low HKUST-1 loadings on a metal-oxide support material, like alumina [45], and even more effective the more the heterogeneous distribution, making up MOF clusters [46]. This could explain the larger improvement registered for drip impregnation materials in case of low MOF loadings, with a more heterogeneous distribution of HKUST-1 on the alumina surface. Although high pressure and low temperature are required to methane hydrates formation, and these conditions do not apply in this case, the arrangement of HKUST-1 on the alumina surface, add to the wetting of the high pore volume of the MOF, may favour methane-water-composite contact in a similar way to the hydrates formation. In fact, several works have demonstrated the improvement in the methane adsorption capacity after wetting the pores of a large-porous material [47]. In general terms, water forms a cage structure in MOF pores with certain affinity towards methane. Furthermore, other authors have demonstrated improvements in the water resistance of HKUST-1 after combining it with other materials in a composite [48,49]. This behaviour is tentatively explained by the surface roughness created by the MOF crystals bound in the matrix, which also agrees with the observation that the drip coating method, causing greater surface heterogeneity, increases stability against humidity.

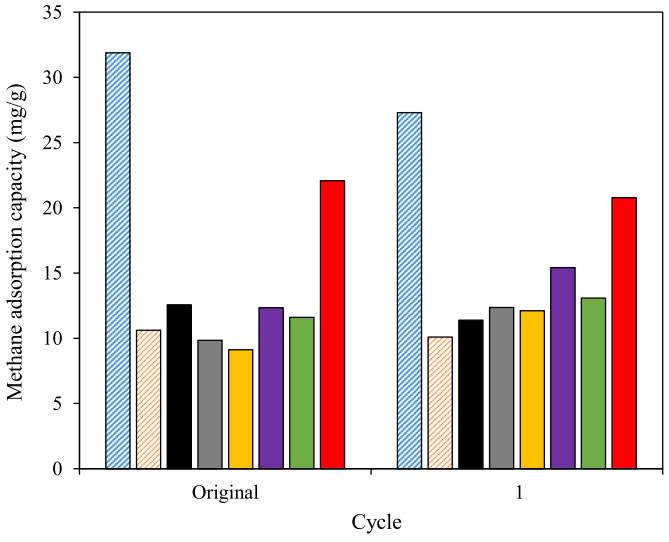

Fig. 6. Variation of methane adsorption capacity after the water-ageing cycle applied to each material. HKUST-1 (blue striped), Al_2O_3 (orange striped), DI_{240} (black), DI_{100v} (grey), DI_{240V} (yellow), S_{240} (purple), S_{240V} (green) and S_{2400V} (red).

This effect was also checked by PXRD, looking for changes on the crystalline structure of the considered materials after the humid adsorption cycle (Fig. S9). The greatest changes are observed for S_{2400V} and DI_{240}, materials with the highest MOF loading. Both materials lose intensity at several peak positions (9.5, 11.6 and 13.4°), in the same way than pure HKUST-1, which shows a large decrease in crystallinity after the water treatment. It is also observed an increase in the amorphous phase after the humid treatment. Further, it is remarkable that both S_{2400V} and DI_{240} maintain the peak at 8.2°. On the other hand, water does not affect alumina peaks at all. Therefore, it is observed that the adsorption performance of composites does not depend on its crystallinity. Similar results are obtained by SEM imaging after the humid treatment, in which it is observed that only HKUST-1 is actually affected, with the appearance of surface fractures (Fig. S10). The rest of the materials do not present any type of surface change observable neither by SEM nor by N_2 adsorption isotherm and pore size distribution.

In this sense, diffuse reflectance infrared spectroscopy (DRIFT) technique has been applied to check changes in the molecular bonds of the composites after the humid treatment (Fig. S11). First, analyses show an adequate impregnation of HKUST-1 on alumina, since although the stretching-bending bands related to alumina (800-1100 cm^{-1}) predominate, bands relative to C═O (1373 and 1618 cm^{-1}) and COO–Cu_2 (1350-1750 cm^{-1}), corresponding to HKUST-1, are also observed in all cases. After the humid treatment, pure HKUST-1 shows some changes, mainly related to a decrease in the intensity of the bands. The presence of moisture weakens the bonds of the structure, and can even cause a structural breakdown. On the other hand, alumina shows an intense peak growth at 1652 cm^{-1} after the water treatment. This peak position can be ascribed to the vibration bands of hydroxyl groups and H–*O*–H from surface-adsorbed water on alumina [23]. This band appears in all composites, showing that water binds to alumina, as no significant changes are observed in the areas related to the MOF. Therefore, despite the decrease in crystallinity, it seems that the MOF maintains its structure and its bond to the alumina after the humid treatment.

Finally, to verify changes in the water-composite interaction, the materials have been exposed to thermal decomposition after humid ageing. Fig. S12 plots the effluent gases (CO_2 and H_2O) profiles obtained by mass spectroscopy. In case of HKUST-1, two main water desorption peaks are observed (343 and 473 K), the first one attributed to physisorbed water. Additionally, it is observed a CO_2 large peak at 593 K, related to the structure decomposition, coincident with thermogravimetry results shown in Fig. S2. For alumina, a large water desorption peak at 473 K is observed, related to chemisorbed water. However, the trend clearly shifts in the case of composites. These materials show two well-differentiated water desorption peaks, 373 and 523 K, except for S_{2400V} and DI_{100v}, materials with the highest and lowest MOF loadings, respectively. The presence of a predominant water desorption peak at 523 K, even in composites with high MOF loadings, suggest the formation of stronger bonds between the water molecule and the surface of composites than on alumina or MOF alone. These results suggest that water is preferentially bound by chemisorption to the alumina surface, which is more water-selective than HKUST-1, thus protecting the MOF structure, although there is also water retained in the porous structure of the MOF. This water wetting the MOF pores causes the enhanced methane adsorption, as seen above. Further, it is noteworthy the absence

of the CO_2 peak from MOF loads of less than 10%, approximately. This is consistent with the results obtained by thermogravimetry, which show greater thermal resistance of composites than HKUST-1. Therefore, the synergy between the MOF and the alumina dramatically increases thermal and moisture stability.

The same humid treatment is applied by three consecutive cycles on all the considered materials in order to confirm the trend (Fig. 7). At the last cycle, HKUST-1 losses about 37% of the original methane adsorption capacity, whereas alumina maintains practically the loss registered at the first cycle, around 5%. The kinetic constants of the proposed kinetic Langmuir model are similar than the corresponding to the tests with the parent composites ($6.1{\cdot}10^{-5}$ s^{-1}), suggesting that adsorption mechanism is essentially the same, despite the losses in the adsorption capacity. This suggests that water blocks OMS for adsorption, decreasing the Langmuir constant, but it does not destroy the MOF structure. Concerning composites, S_{2400V} and DI_{240} loss again an important part of their adsorption capacity after the third cycle, 27.3 and 15.8%, respectively. Again, at low MOF loadings on the composites, the water effect is the opposite, and the methane adsorption capacity continues above the original capacity. In fact, in some composites, such as DI_{240V}, it even increases from the first to the third cycle. Therefore, these results confirm the previously proposed assumption. Table 4 shows the adsorption capacities registered with cycles.

Finally, Fig. 8 relates the capacity loss after the third cycle with the MOF content in each composite. As seen, there is a gap between DI_{240} and S_{240}, and it goes from a loss of 15.8% to a capacity gain of 18.9% after three humid cycles. Therefore, it can be indicated that in this gap, which include around 9% of MOF load variation, an arrangement of HKUST-1 occurs on the alumina surface that greatly favours the methane-water-composite interaction. Below this value, and regardless of the impregnation method, the presence of water seems favourable in the methane adsorption by HKUST-1/Al_2O_3 composites, reaching even an improvement of 38% in the case of DI_{240V}. These results suggest that the performance improvement occurs only for low MOF loads, and with larger intensity in the case of a more heterogeneous distribution (drip impregnation), which agrees with the assumptions previously made.

4. Conclusions

This study has successfully demonstrated the significant advantages of HKUST-1/Al_2O_3 composites compared to the pristine MOF. These advantages primarily include the ability to operate with minimal pressure drop in fixed-bed adsorption and improved stability in the presence of water.

Different HKUST-1/Al_2O_3 composites (prepared using various preparation methods and MOF loadings) have been tested for methane adsorption. Alumina particles were selected for their large particle size and high hydrophilicity, which can reduce the pressure drop in a fixed-bed and protect the MOF from water, respectively. Composites with a high MOF load follow the same trend as pristine HKUST-1, although with lower capacity losses. Surprisingly, in the case of composites with HKUST-1 loads lower than 9%, the presence of water increases the methane adsorption capacity by up to 38% compared to the original.

This effect is more striking in the case of drip impregnation composites, with a more heterogeneous distribution on the MOF, so higher surface roughness, giving rise to clusters that follow a similar principle to the methane-hydrate formation, but at milder conditions. The alumina selectivity towards water protects the HKUST-1 structure. In addition, thermal decomposition essays show an increase in the thermal stability of the MOF when forming the composites, confirming the synergy between the MOF and the alumina, strengthening the structure. Further, pressure drop is negligible in all composite cases. Results open the possibility of using these composites in actual operations.

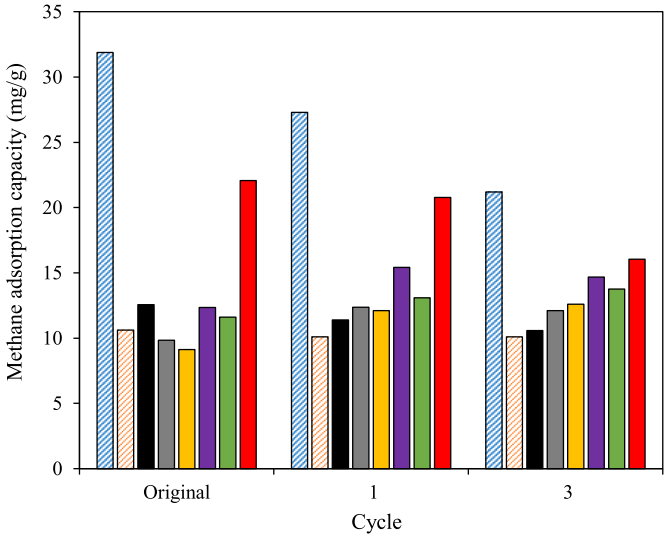

Fig. 7. Variation of methane adsorption capacity through the water-ageing cycles applied to each material. HKUST-1 (blue striped), Al_2O_3 (orange striped), DI_{240} (black), DI_{100v} (grey), DI_{240V} (yellow), S_{240} (purple), S_{240V} (green) and S_{2400V} (red).

Table 4
Variation in methane adsorption capacity after one and three consecutive cycles in presence of water (100% RH).

Material	Original (mg/g)	1st cycle (mg/g)	3rd cycle (mg/g)
HKUST-1	32.1 ± 0.6	27.3 ± 0.6	21.2 ± 0.6
Al_2O_3	10.6 ± 0.2	10.1 ± 0.3	10.1 ± 0.2
DI_{100v}	9.84 ± 0.3	12.4 ± 0.6	12.1 ± 0.2
DI_{240}	12.5 ± 0.2	11.4 ± 0.1	10.6 ± 0.3
DI_{240V}	9.12 ± 0.3	12.1 ± 0.4	12.6 ± 0.2
S_{240}	12.3 ± 0.6	15.4 ± 0.5	14.7 ± 0.1
S_{2400V}	22.1 ± 0.4	20.7 ± 0.4	16.1 ± 0.3
S_{240V}	11.6 ± 0.2	13.1 ± 0.1	13.7 ± 0.2

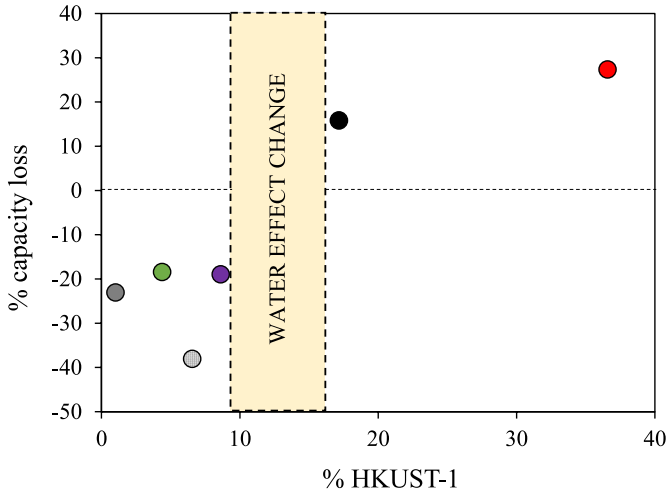

Fig. 8. Relation between the methane adsorption capacity loss after three cycles of water ageing (24 h, 100% RH) on a fixed-bed and the HKUST-1 load on each composite. The shaded area indicates the trend change. DI_{240} (black), DI_{100v} (grey), DI_{240V} (yellow), S_{240} (purple), S_{240V} (green) and S_{2400V} (red).

CRediT authorship contribution statement

David Ursueguía: Writing – original draft, Investigation, Formal analysis, Data curation. **Eva Díaz:** Writing – review & editing, Visualization, Supervision, Project administration. **Salvador Ordóñez:** Writing – review & editing, Visualization, Supervision, Funding acquisition,

Conceptualization.

Declaration of competing interest

The authors declare that they have no known competing financial interests or personal relationships that could have appeared to influence the work reported in this paper.

Data availability

Data will be made available on request.

Acknowledgements

This work was supported by the Government of Asturias (Spain), (contract GRUPIN AYUD/2021/50450) and by the Spanish Agency for Research (PID2020-112587RB-I100).

David Ursueguía acknowledges the Spanish Government for the PhD grant that supports his research (FPU18/01448). Authors would like to acknowledge the technical support provided by *Servicios Científico-Técnicos de la Universidad de Oviedo*.

Appendix A. Supplementary data

Supplementary data to this article can be found online at https://doi.org/10.1016/j.micromeso.2023.112712.

References

[1] K. Nath, A. Ahmed, D. Siegel, A. Matzger, Angew. Chem. 134 (2022), e202203575, https://doi.org/10.1002/ange.202203575.
[2] D. Ursueguía, E. Díaz, A. Vega, S. Ordóñez, Sep. Purif. Technol. 251 (2020), 117374, https://doi.org/10.1016/j.seppur.2020.117374.
[3] E. Tsalaporta, J. MacElroy, Heliyon 6 (2020), E04883, https://doi.org/10.1016/j.heliyon.2020.e04883.
[4] A. Domán, O. Czakkel, L. Porcar, J. Madarász, E. Geissler, K. László, Appl. Surf. Sci. 480 (2019) 138–147, https://doi.org/10.1016/j.apsusc.2019.02.177.
[5] J. Canivet, A. Fateeva, Y. Guo, B. Coasne, D. Farrusseng, Chem. Soc. Rev. 43 (2014) 5594–5617, https://doi.org/10.1039/C4CS00078A.
[6] B. Ray, S. Churipard, S. Peter, J. Math. Chem. A 9 (2021) 26498–26527, https://doi.org/10.1039/D1TA08862A.
[7] P. Goyal, A. Paruthi, D. Menon, R. Behara, A. Jaiswal, K. V, A. Kumar, V. Krishnan, S. Misra, Chem. Eng. J. 430 (2022), 133088, https://doi.org/10.1016/j.cej.2021.133088.
[8] Y. Wu, Y. Sun, J. Xiao, X. Wang, Z. Li, ACS Sustain. Chem. Eng. 7 (2019) 1557–1563, https://doi.org/10.1021/acssuschemeng.8b05321.
[9] M. Kanno, T. Kitao, T. Ito, K. Terashima, RSC Adv. 11 (2021) 22756–22760, https://doi.org/10.1039/D1RA00942G.
[10] R. Pan, Y. Tang, Y. Guo, J. Shang, L. Zhou, W. Dong, D. He, Microporous Mesoporous Mater. 323 (2021), 111197, https://doi.org/10.1016/j.micromeso.2021.111197.
[11] M. Majaz, T. Cendak, G. Buscarino, M. Todaro, N. Logar, J. Math. Chem. A 5 (2017) 22305–22315, https://doi.org/10.1039/C7TA04959E.
[12] P. Jagódka, K. Matus, A. Lamacz, Molecules 27 (2022) 7082, https://doi.org/10.3390/molecules27207082.
[13] S. Xie, W. Monnens, K. Wan, W. Zhang, W. Guo, M. Xu, I. Vankelecom, X. Zhang, J. Fransaer, Angew. Chem. 133 (2021) 25154–25161, https://doi.org/10.1002/ange.202108485.
[14] T. Wang, A. Wright, W. Hoover, K. Stoffel, R. Richardson, S. Rodriguez, R. Flores, J. Siegfried, N. Vermeulen, P. Fuller, M. Weston, O. Farha, W. Morris, ACS Appl. Mater. Interfaces 13 (2021) 52106–52112, https://doi.org/10.1021/acsami.1c09619.
[15] D. Ursueguía, C. Daniel, C. Collomb, C. Cardenas, D. Farrusseng, E. Díaz, S. Ordóñez, Langmuir 38 (2022) 14465–14474, https://doi.org/10.1021/acs.langmuir.2c02332.
[16] D. Ursueguía, E. Díaz, S. Ordóñez, Nanomaterials 10 (2020) 1089, https://doi.org/10.3390/nano10061089.
[17] Z. Wang, L. Liu, Z. Li, N. Goyal, T. Du, J. He, G. Li, Energy Fuels 36 (2022) 2927–2944, https://doi.org/10.1021/acs.energyfuels.1c03426.
[18] M. Hamid, Y. Qian, R. Wei, Z. Li, Y. Pan, Z. Lai, H. Jeong, J. Membr. Sci. 640 (2021), 119802, https://doi.org/10.1016/j.memsci.2021.119802.
[19] J. Dong, P. Li, H. Guan, C. Ge, Y. Bai, Y. Zhao, X. Zhang, Inorg. Chem. Commun. 117 (2020), 107975, https://doi.org/10.1016/j.inoche.2020.107975.
[20] H. Etemadi, S. Afsharkia, S. Zinatloo-Ajabshir, E. Shokri, Polym. Eng. Sci. 61 (2021) 2364–2375, https://doi.org/10.1002/pen.25764.
[21] O. Shekhah, J. Liu, R. Fischer, C. Wöll, Chem. Soc. Rev. 40 (2011) 1081–1106, https://doi.org/10.1039/C0CS00147C.
[22] J. Gascon, S. Aguado, F. Kapteijn, Microporous Mesoporous Mater. 113 (2008) 132–138, https://doi.org/10.1016/j.micromeso.2007.11.014.
[23] L. Qin, Y. Zhou, D. Li, L. Zhang, Z. Zhao, Z. Zuhra, C. Mu, Ind. Eng. Chem. Res. 55 (2016) 7249–7258, https://doi.org/10.1021/acs.iecr.6b01001.
[24] D. Atinafu, S. Chang, U. Berardi, K. Kim, S. Kim, J. Hazard Mater. 402 (2021), 123695, https://doi.org/10.1016/j.jhazmat.2020.123695.
[25] Y. Yang, L. Ge, V. Rudolph, Z. Zhu, Dalton Trans. 43 (2014), 70287036, https://doi.org/10.1039/C3DT53191K.
[26] J. Yu, T. Ma, S. Lu, Phys. Chem. Chem. Phys. 13 (2011) 3491–3501, https://doi.org/10.1039/C0CP01139H.
[27] Q. Liu, L. Jin, W. Sun, Chem. Commun. 48 (2012) 8814–8816, https://doi.org/10.1039/c2cc34192a.
[28] R. Sule, A. Mishra, Appl. Sci. 9 (2019) 4407, https://doi.org/10.3390/app9204407.
[29] T. Saleh, Chem. Eng. J. 404 (2021), 126987, https://doi.org/10.1016/j.cej.2020.126987.
[30] N. Emami, M. Farhadian, A. Solaimany, S. Tangestaninejad, Int. J. Environ. Sci. Technol. (2022), https://doi.org/10.1007/s13762-022-04679-7.
[31] S. Denning, A. Majid, J. Lucero, J. Crawford, M. Carreon, C. Koh, ACS Appl. Mater. Interfaces 12 (2020) 53510–53518, https://doi.org/10.1021/acsami.0c15675.
[32] F. Martak, M. Hafiz, D. Sulistiono, A. Rosyidah, Y. Kusumawati, R. Ediati, Nano-Struct. Nano-Objects 27 (2021), 100773, https://doi.org/10.1016/j.nanoso.2021.100773.
[33] X. Ma, S. Peng, W. Li, H. Liu, Y. Chen, CrystEngComm 20 (2018) 407–411, https://doi.org/10.1039/C7CE01922J.
[34] C. Zheng, H. Ren, Z. Cui, F. Chen, G. Hong, J. Alloys Compd. 477 (2009) 333–336, https://doi.org/10.1016/j.jallcom.2008.09.201.
[35] E. Moumen, L. Bazzi, S. El Hankari, Process Saf. Environ. Protect. 160 (2022) 502–512, https://doi.org/10.1016/j.psep.2022.02.034.
[36] W. Zhao, Y. Long, Y. He, J. Cai, M. Liu, Microporous Mesoporous Mater. 344 (2022), 112207, https://doi.org/10.1016/j.micromeso.2022.112207.
[37] K. Liu, Y. Zheng, G. Jia, M. Yang, Y. Song, N. Guo, H. You, J. Solid State Chem. 183 (2010) 2309–2316, https://doi.org/10.1016/j.jssc.2010.07.040.
[38] W. Zhang, X. Wen, S. Yang, Y. Berta, Z. Wang, Adv. Mater. 15 (2003) 822–825, https://doi.org/10.1002/adma.200304840.
[39] K. Okada, R. Ricco, Y. Tokudome, M. Styles, A. Hill, M. Takahashi, P. Falcaro, Adv. Funct. Mater. 24 (2014) 1969–1977, https://doi.org/10.1002/adfm.201303303.
[40] D. Ursueguía, E. Díaz, S. Ordóñez, Microporous Mesoporous Mater. 298 (2020), 110048, https://doi.org/10.1016/j.micromeso.2020.110048.
[41] J. Wang, X. Guo, J. Hazard Mater. 390 (2020), 122156, https://doi.org/10.1016/j.jhazmat.2020.122156.
[42] N. Torasso, A. Vergara, P. Rivas, C. Huck, A. Larrañaga, A. Fernández, S. Cerveny, S. Goyanes, J. Environ. Chem. Eng. 9 (2021), 104664, https://doi.org/10.1016/j.jece.2020.104664.
[43] J. Kim, S. Yoo, Y. Kong, S. Cho, E. Lee, Langmuir 37 (2021) 11301–11308, https://doi.org/10.1021/acs.langmuir.1c01859.
[44] S. Denning, A. Majid, J. Crawford, J. Wells, M. Carreon, C. Koh, Fuel 325 (2022), 124920, https://doi.org/10.1016/j.fuel.2022.124920.
[45] V. Smirnov, A. Manakov, S. Lyrshchikov, T. Rodionova, V. Dyrdin, Z. Ismagilov, J. Mol. Liq. 328 (2021), 115486, https://doi.org/10.1016/j.molliq.2021.115486.
[46] A. Nesterov, A. Reshetnikov, A. Manakov, T. Rodionova, E. Paukshtis, I. Asanov, S. Bardakhanov, A. Bulavchenko, J. Mol. Liq. 204 (2015) 118–125, https://doi.org/10.1016/j.molliq.2015.01.037.
[47] H. Liu, S. Zhan, P. Guo, S. Fan, S. Zhang, Chem. Eng. J. 349 (2018) 775–781, https://doi.org/10.1016/j.cej.2018.05.150.
[48] J. DeCoste, M. Denny, G. Peterson, J. Mahle, S. Cohen, Chem. Sci. 7 (2016) 2711–2716, https://doi.org/10.1039/C5SC04368A.
[49] Z. Zhang, W. Huang, X. Li, X. Wang, Y. Zheng, B. Yan, C. Wu, Inorg. Chem. Commun. 146 (2022), 110063, https://doi.org/10.1016/j.inoche.2022.110063.